Plasmon-enhanced nanoporous $BiVO_4$ photoanodes for efficient photoelectrochemical water oxidation

Plasmon-enhanced nanoporous BiVO$_4$ photoanodes for efficient photoelectrochemical water oxidation

Jiayong Gan[1,2], Bharath Bangalore Rajeeva[1], Zilong Wu[1], Daniel Penley[1], Chaolun Liang[2], Yexiang Tong[2,3] and Yuebing Zheng[1,3]

[1] Department of Mechanical Engineering, Materials Science and Engineering Program, and Texas Materials Institute, The University of Texas at Austin, Austin, Texas 78712, USA
[2] KLGHEI of Environment and Energy Chemistry, MOE of the Key Laboratory of Bioinorganic and Synthetic Chemistry, School of Chemistry and Chemical Engineering, Sun Yat-Sen University, Guangzhou 510275, People's Republic of China

E-mail: chedhx@mail.sysu.edu.cn (YT) and zheng@austin.utexas.edu

CrossMark

Abstract

Conversion of solar irradiation into chemical fuels such as hydrogen with the use of a photoelectrochemical (PEC) cell is an attractive strategy for green energy. The promising technique of incorporating metal nanoparticles (NPs) in the photoelectrodes is being explored to enhance the performance of the photoelectrodes. In this work, we developed Au-NPs-functionalized nanoporous BiVO$_4$ photoanodes, and utilized the plasmonic effects of Au NPs to enhance the photoresponse. The plasmonic enhancement leads to an AM 1.5 photocurrent of 5.1 ± 0.1 mA cm^{-2} at 1.23 V versus a reverse hydrogen electrode. We observed an enhancement of five times with respect to pristine BiVO$_4$ in the photocurrent with long-term stability and high energy-conversion efficiency. The overall performance enhancement is attributed to the synergy between the nanoporous architecture of BiVO$_4$ and the plasmonic effects of Au NPs. Our further study reveals that the commendable photoactivity arises from the different plasmonic effects and co-catalyst effects of Au NPs.

S Online supplementary data available from stacks.iop.org/NANO/27/235401/mmedia

(Some figures may appear in colour only in the online journal)

Introduction

With the ever-increasing demand for energy, there is a pressing need to explore additional viable sources. Among the various available alternatives, solar energy is an attractive option to provide long-term sustainable energy. Using the photoelectrochemical (PEC) cell, which utilizes sunlight to extract hydrogen and oxygen from water, is a promising strategy for capturing and chemically storing solar energy while tackling current environmental issues [1, 2]. Though the

concept of PEC cells has been explored since 1972 [3], the real-life incorporation of robust and efficient cells has been challenging. One of the main barriers is the challenge of developing cheap, highly-efficient and stable photoanode materials. Metal oxides such as hematite (α-Fe$_2$O$_3$) [4, 5], zinc oxide (ZnO) [6, 7] and bismuth vanadate (BiVO$_4$) [8] are being explored as potential photoanodes due to their relatively high stability in aqueous media. Among these photoanode candidates, BiVO$_4$ is being researched for water oxidation due to its direct band gap of 2.4 eV and suitable band position for oxygen evolution, resulting in a low onset potential and the utilization of the blue portion of the visible spectrum

---

[3] Authors to whom any correspondence should be addressed.

[9, 10]. However, the performance achieved with a BiVO$_4$ photoanode has not matched expectations. The main hindrance is the poor electron-hole separation efficiency, resulting in significant recombination in the bulky BiVO$_4$ [11]. Slow oxygen evolution kinetics due to poor charge transport is another limitation, which is tackled with cobalt-based co-catalysts [12]. Doping and morphology modification have also been reported to aid in the electron transport within the material and to reduce the recombination probability [13, 14]. An effective strategy with numerous advantages for morphology modification is the creation of nanostructured BiVO$_4$. The nanostructures can enhance charge transport and electron-hole separation, leading to BiVO$_4$ with superior PEC performance [15–17].

Over the past decade, plasmonic nanoparticles (NPs) have been extensively explored due to their attractive optical properties [18–21]. They have been used for an array of applications, including surface-enhanced spectroscopy [22, 23], plasmonic lasers [24], biomedical imaging [25], biosensing [26], and metamaterials [27]. In recent years, there has been a growing interest in exploiting plasmonic nanomaterials to improve the efficiency of photochemical and photovoltaic reactions [28]. In particular, the plasmonic enhancement of solar water splitting is being actively pursued [29–31]. For most of the PEC applications, Au NPs are incorporated into the semiconductors due to their chemical stability and broad optical response from visible to infrared [32]. The dominant mechanisms for the plasmonic enhancement of chemical reactions include (i) plasmon resonance energy transfer (PRET) from metal NPs to the adjacent semiconductors, (ii) hot-electron injection, where electrons are generated and injected into the conduction band (CB) of semiconductors upon the non-irradiative decay of surface plasmons, (iii) plasmonic heating, and (iv) local electromagnetic field concentration for the enhanced light absorption by semiconductors [29, 30, 33]. With one or more of these mechanisms, Au NPs have been shown to improve the water-splitting performance on various materials such as TiO$_2$ [34, 35], ZnO [36], Fe$_2$O$_3$ [37] and BiVO$_4$ [38, 39]. Hot-electron injection enhancement is particularly promising among the various approaches. Pu and coworkers have established photoactivity over the entire UV–visible spectrum on TiO$_2$ by employing Au NPs [40]. The role of hot electrons in chemical reactions on ZnO has also been studied [36]. Recently, the charge transfer from NPs to BiVO$_4$ has been attributed to the enhanced PEC performance of inverse opal BiVO$_4$ decorated with Au NPs [38]. In spite of the numerous experiments that exhibit the consistent plasmonic enhancement of PEC performance, mechanistic understanding of the enhancement mechanisms has been inconsistent due to the difficulty in decoupling the different mechanisms in the measurements. Therefore, experiments that aim to probe, understand and optimize each of the plasmonic enhancement mechanisms are highly desired in order to maximize the performance of PEC cells.

In this work, we fabricated nanoporous BiVO$_4$ decorated with Au NPs to work as photoanodes. The photoanodes exhibit several advantages, including an improved photocurrent response and solar energy-conversion efficiency. With the high surface areas of nanoporous BiVO$_4$ and the uniform dispersion of Au NPs on the nanostructure surfaces, we have managed to synergize multiple enhancement mechanisms for the Au-BiVO$_4$ systems. These enhanced mechanisms include an enhanced charge and carrier collection, a plasmon-induced electron and energy transfer, a plasmon-enhanced electromagnetic field and a co-catalyst effect. The cumulative effect is the maximal utilization of the generated charges. As a result, an AM 1.5G photocurrent density of $5.1 \pm 0.1 \, \text{mA cm}^{-2}$ at 1.23 V versus a reverse hydrogen electrode (RHE) was achieved along with a >99% Faraday efficiency, which is among the state-of-the-art systems [38]. It should be noted that no surface electrocatalysts were integrated with the photoanode. The Au-BiVO$_4$ photoanodes in combination with their simple electrochemical and chemical deposition techniques lead to robust, high-performance solar water oxidation in tandem or hybrid PEC cells. Moreover, we have analyzed the plasmonic contributions from hot-electron injection, an enhanced electromagnetic field and PRET, and concluded that they play a major role in the plasmonic enhancement of PEC performance. Our work incorporates hot-electron injection and further mechanistic analysis of the various enhancement mechanisms in order to pave the way towards the rational design of hybrid photoanodes with optimal performance.

Results and discussion

We have prepared a series of nanostructured BiVO$_4$ electrodes with variable loadings of Au NPs and comparatively studied their PEC performances. As described in the 'Materials and Methods' section, an array of BiOI nanoflakes was synthesized on the fluorine-doped tin oxide (FTO) glass substrates to serve as templates for the preparation of the nanoporous BiVO$_4$. Scanning electron microscope (SEM) images in figure 1(a) show the two-dimensional (2D) morphology of a collection of randomly oriented BiOI nanoflakes (ca. 20 nm in thickness) with voids between them. These voids limit the grain growth of BiVO$_4$ converted from BiOI, leading to a high surface area of the BiVO$_4$ films. Figure 1(b) shows the BiVO$_4$ electrodes that form a 2D nanoporous network consisting of numerous spherical NPs (average diameter of 70 ± 10 nm). This network of BiVO$_4$ NPs with their dimensions smaller than the hole diffusion length is expected to lead to highly-efficient electron–hole separation [41]. Such 2D nanoporous structures have proved to be superior for PEC and photovoltaic applications due to their enhanced capability of charge carrier separation and collection [8]. The spherical particles have small radii, and the minority carriers that are generated therein can diffuse to their surfaces before they recombine.

The deposition of Au on the BiVO$_4$ substrate was carried out for different durations, i.e. 1 h, 3 h, 6 h, 12 h, and 24 h. Figures 1(c) and (d) show the SEM images for BiOI and BiVO$_4$ films after the Au deposition for 12 h. The formation of the Au NPs with an average of 30 nm in diameter can be
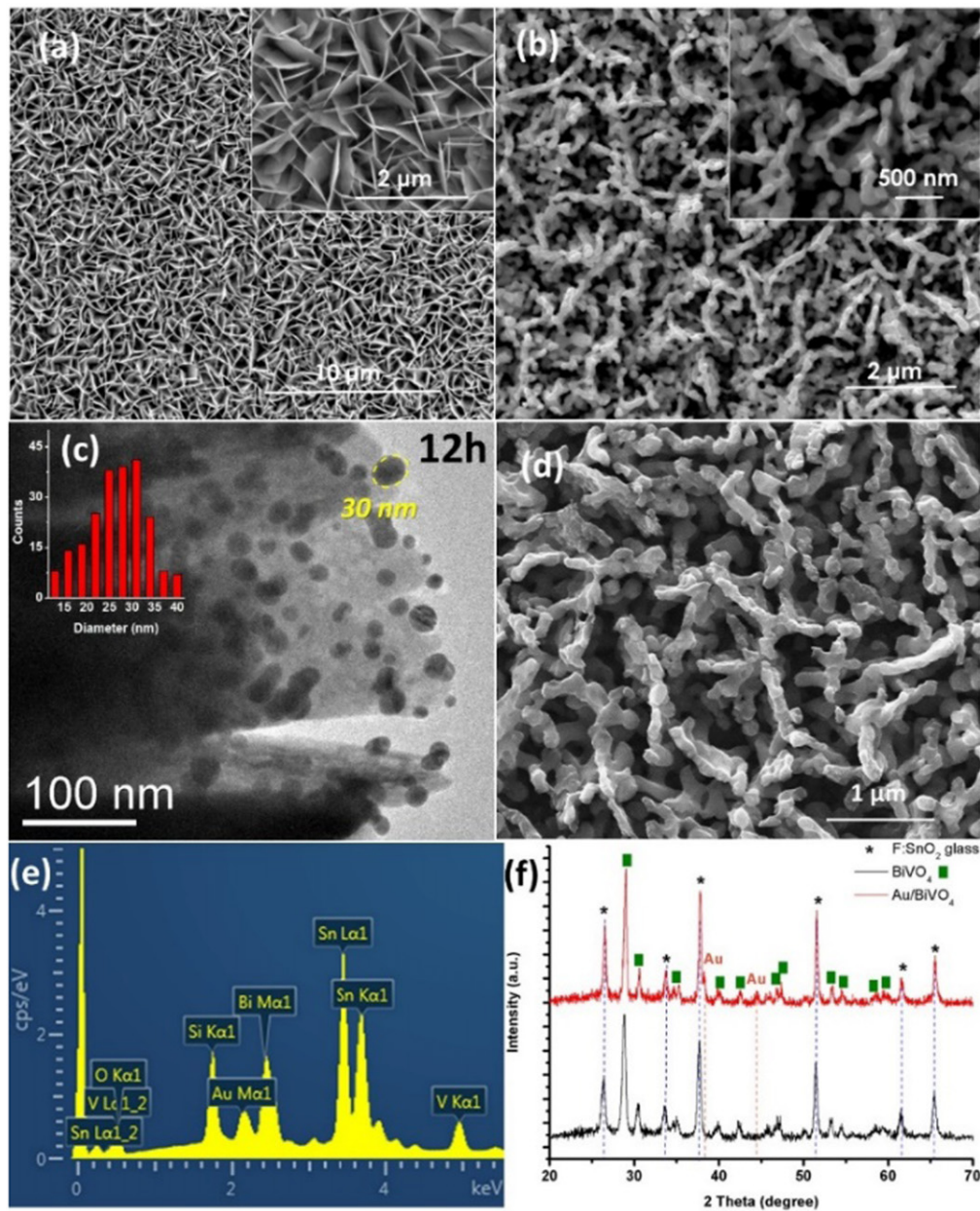
Figure 1. Scanning electron micrographs of (a) BiOI template at low and high magnification (inset) and (b) BiVO$_4$ at low magnification and high magnification (inset). (c) and (d) TEM and SEM images of BiVO$_4$ samples with a loading time of 12 h. (e) Energy dispersive spectroscopy (EDS) spectrum of an Au-BiVO$_4$ sample showing the presence of Au. (f) X-ray diffractometer (XRD) spectra for pristine BiVO$_4$ and Au-BiVO$_4$. A single Au NP with a diameter of 30 nm and size distribution are indicated in the inset of (c).

clearly seen on the BiOI films (see figure 1(c)). We also observed a gradual increase in the NP distribution as the Au deposition time is increased. The Au NPs start to aggregate especially in the case of the 24 h sample, which may lead to the formation of a thin layer of Au NPs (supplementary figure S1). In order to further confirm the chemical compositions of the films, we performed EDS on the BiVO$_4$ samples after the Au deposition. A distinct Au peak is observed besides the expected Bi, V and O peaks (figure 1(e)). The corresponding XRD spectrum (figure 1(f)) also confirms the scheelite-monoclinic structure (JCPDS #:14-0688) of BiVO$_4$ and the existence of cubic gold (JCPDS #:2-1095), further verifying the crystalline phase of Au-BiVO$_4$.

In order to investigate the effects of Au NPs on the optical properties of the BiVO$_4$, we measured the optical diffuse reflectance spectra of pristine BiVO$_4$ and Au-BiVO$_4$ with different Au loadings (figure 2(a)). It has been known that pristine BiVO$_4$ has an electronic band gap of 2.4 eV, which corresponds to 515 nm in wavelength, and exhibits an obvious drop in the absorption spectrum (figure 2(a)). A characteristic feature of Au NPs exploited for most of their applications is the excitation of localized surface plasmon resonances (LSPRs), the light-coupled coherent oscillation of free electrons in the NPs [42]. Due to their dependence on the NP shape and size, the LSPRs can be tuned to overlap with the semiconductor absorption wavelengths to achieve
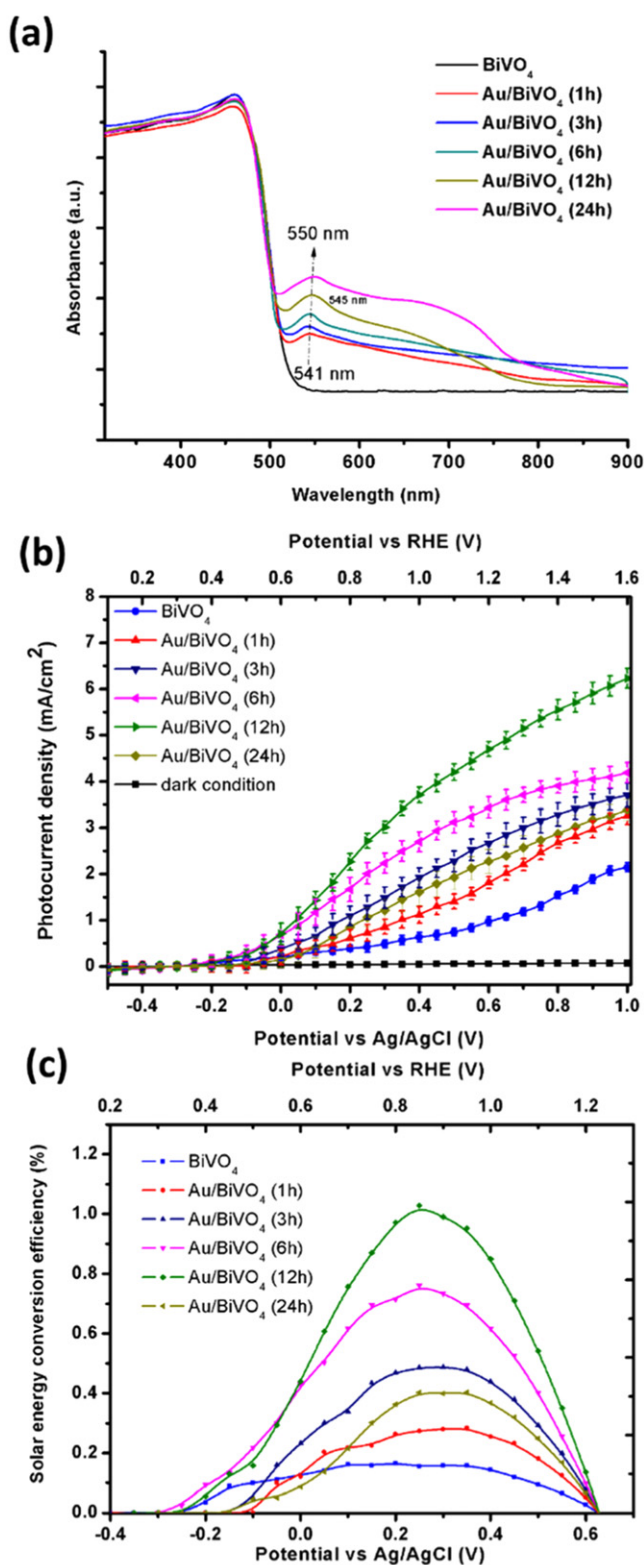
Figure 2. (a) Diffuse reflectance spectra of a pristine $BiVO_4$ photoelectrode and Au-$BiVO_4$ photoelectrodes with different NP loading times. (b) Linear-sweep voltammograms of pristine $BiVO_4$ and Au-$BiVO_4$ photoelectrodes performed in a 0.2 M aqueous Na_2SO_4 with a pH of 7 under a solar simulator (AM 1.5, 100 mW cm^{-2}). The dark scan is included. (c) Calculated solar energy-conversion efficiencies for the different photoelectrodes. The η was evaluated based on a three-electrode system.

enhanced physical and chemical processes. In figure 2(a), with the increase in deposition time, the absorbance that originated from the surface plasmon resonance of Au NPs (~541 nm) gradually increased, suggesting that the loading of Au can be effectively controlled to optimize the absorption conditions for the PEC reactions. As expected, the absorbance of Au-$BiVO_4$ (24 h) is maximum at the LSPRs' frequency. The increased loading time also causes a redshift (from 541 to 550 nm) in the LSPRs' peak wavelength with an increased bandwidth. The redshift is attributed to the progressive deposition of Au particles upon the $BiVO_4$. The peak shift may be caused by the increased size of Au NPs and the decreased inter-particle distance. Notably, the 24 h sample showed a shoulder at approximately 680 nm in addition to the major plasmon resonance peak. This bimodal distribution may come from the same LSPRs' absorption. This phenomenon is attributable to the formation of Au NPs aggregation with very low inter-particle distance resulting in interactions between neighboring atoms [43].

Electrochemical measurements were performed systematically to evaluate the plasmonic effects on the PEC performance of $BiVO_4$ loaded with different amounts of Au NPs. The PEC properties of the Au-$BiVO_4$ photoanodes were examined in 0.2 M Na_2SO_4 aqueous solution at pH = 7 under AM 1.5G illumination and dark conditions. The typical linear sweep voltammetry of the pristine and Au-$BiVO_4$ photoanodes (figure 2(b)) was conducted with back-side illumination. The data points and error bars depict the average and standard deviation values from the measurements of multiple samples. Throughout the deposition process, the mean Au NPs sizes are found to be concentrated in 25–32 nm (see figure S1). Within this range, the particle distribution increased as the Au loading time prolonged. The dark scan led to a negligible current. Under illumination, $BiVO_4$ electrodes exhibit an increased photocurrent as a function of the loading of Au NPs up to 12 h. A similar trend can be found in the front-side illumination (see figure S2). The $BiVO_4$ electrode with a NP loading time of 12 h yielded a pronounced photocurrent, which started from −0.22 V and increased to 5.10 mA cm^{-2} when +1.23 V versus RHE was applied. This corresponds to an almost five times increase over pristine $BiVO_4$ (1.1 mA cm^{-2} at the same potential). The increase suggests that the decoration by Au NPs promoted the harvesting of solar light via plasmonic enhancement. Moreover, the current onset potential is shifted cathodically (see figure S3), implying that both the kinetics of oxygen evolution as well as the surface recombination of electrons and holes were improved due to the plasmonic enhancement and the electrocatalytic effect of Au. However, a drastic decrease in the photocurrent occurs at the $BiVO_4$ electrode with the Au loading time of 24 h; this arises from the blocking effect of the larger number of Au NPs on the surfaces [36]. Figure S2 shows the data for the front-side illumination measurement. Upon increasing the loading time from 12 h to 24 h, the blocking effect of the incident light by the Au NPs is also doubled. (Figure S4 shows the presence of Au aggregates.) Additionally, Au NPs can also behave as trap centers for photoelectrons [36] and collect some photogenerated
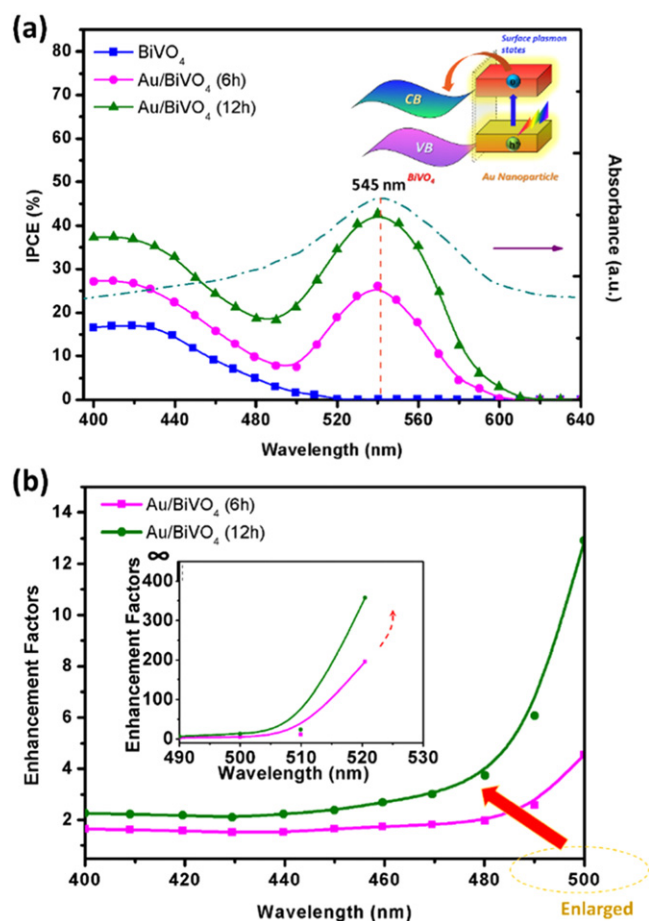
Figure 3. (a) IPCE spectra of pristine $BiVO_4$ and Au-$BiVO_4$ with Au loading times of 6 h and 12 h. The measurements were carried out at an applied potential of $+1.0$ V versus RHE under a solar simulator (AM 1.5, 100 mW cm^{-2}). The optical absorption spectrum of Au NPs is included. The inset illustrates the plasmon-induced hot-electron injection mechanism. (b) IPCE enhancement factors for Au-$BiVO_4$ with Au loading times of 6 h and 12 h. Inset is a zoom-in for the wavelength ranging from 490 nm to 530 nm. The factor approaches infinity above 530 nm since pristine $BiVO_4$ has no photoactivity.

electrons from the $BiVO_4$; this results in a negative effect on the photoresponse. As a result, the optimal performance in the $BiVO_4$ electrode with the loading time of 12 h arises from the balance between the plasmonic enhancement and the blocking effect of Au NPs.

For further insights into the photoelectrode properties, we have calculated the solar energy-conversion efficiency (η) assuming a 100% Faradaic efficiency, which reflects the photoconversion efficiency based on equation (2). As shown in figure 2(c), η exhibits a similar trend to the photocurrent as a function of the Au loading time. Compared to pristine $BiVO_4$ at 0.80 V, the η of Au-$BiVO_4$ (1 h ∼ 12 h) is enhanced almost five times from 0.15% to 1.00%. It is worth reiterating that no surface electrocatalysts were added onto the electrodes. In the presence of an appropriate oxygen evolution catalyst, we expect the photocurrent onset potential to be even lower.

Figure 3(a) shows the incident photon-to-current conversion efficiency (IPCE) to quantitatively investigate the relations between the photoactivity and the light absorption. All the electrodes were measured at 1.0 V versus RHE under the same conditions. The IPCE spectrum of pristine $BiVO_4$ exhibits a photoresponse up to 520 nm in accordance with the absorption edge of $BiVO_4$. A significant increase in the performance is observed upon the addition of Au NPs. Further, we observed additional photoactivity in the Au-$BiVO_4$ samples up to 600 nm where the optical absorption of Au NPs starts to subside. A similar trend was observed in the front-side illumination (figure S5). To investigate the mechanisms of the increased photoactivity, we consider and analyze the different plasmonic phenomena. We can eliminate the effect of resonant photon scattering by NPs in increasing the path length of photons in $BiVO_4$ since scattering for Au NPs smaller than 50 nm is minimal (see figure S6) [44]. We can also exclude the plasmonic heating, since the thermal energy caused by plasmonic heating is much less than the amount of energy required for the water splitting (1.23 eV) [34]. Further, the cyclic voltammetry indicates that the Au NPs are not oxidized (figure S8). On the other hand, there is a small overlap between the optical absorption spectra of the pristine $BiVO_4$ and that of the Au NPs, indicating that both PRET and the plasmon-enhanced light absorption by $BiVO_4$ can occur in the composites [29]. The latter is due to the concentrated and enhanced electromagnetic fields at the nanoporous structure by the LSPRs in the Au NPs. Other possible contributors to the enhanced photocurrent can include the plasmon-induced hot-carrier injection from Au NPs to $BiVO_4$. Upon the decay of the LSPRs, hot electrons are injected to the CB of $BiVO_4$, because photoexcited plasmons promote single electrons to high-energy states in the Au NPs and the energy of hot electrons is higher than the CB of $BiVO_4$ (inset in figure 3(a)).

Further, we quantify the enhancement factors by dividing the IPCE values of the 6 h and 12 h samples with those of pristine $BiVO_4$ (see figure 3(b)). There exists an IPCE peak at 420 nm because of the photoactivity of $BiVO_4$ in this range. The enhancement factors are limited to about 1.2 from 400 to 450 nm. However, the factors start to increase drastically due to stronger plasmonic effects, which match well with the wavelength of Au NP LSPRs (figure 3(a)). Beyond 520 nm, the enhancement factor rises steeply to over 100. Due to the negligible contribution from the semiconductor above 543 nm, the enhancement factor approaches infinity. Therefore, the performance improvement can be mainly attributed to PRET, the plasmon-enhanced light absorption and the hot-electron injection. The plasmonic effects in the Au-$BiVO_4$ system can be maximized via adopting an optimized amount of Au NPs.

To verify the contributions from hot-electron injection and PRET, the Au-$BiVO_4$ (12 h) photoelectrode was further tested under on-off cycle illumination with the solar spectrum and a 525 nm long-pass filter (figure 4(a)). Since the activity of $BiVO_4$ is up to 520 nm, we plot the photoresponse of pristine $BiVO_4$ as a control, which is overlapped with the photoresponse of Au-$BiVO_4$. The difference in the
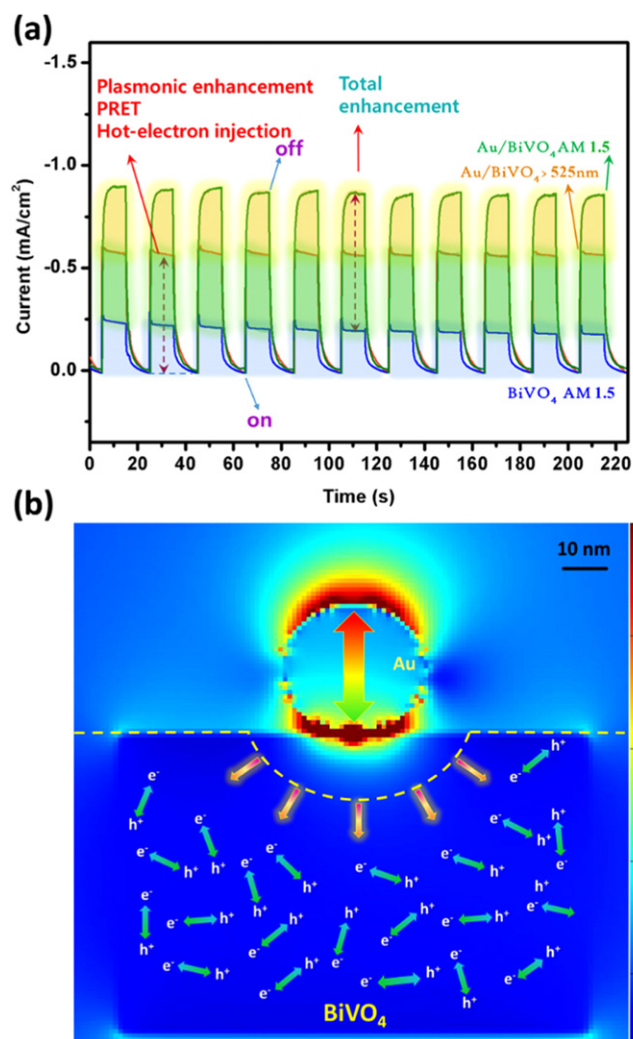
Figure 4. (a) Amperometric current−time (*I*–*T*) curves of Au-BiVO₄ (Au loading time of 12 h) and pristine BiVO₄ with on/off cycles under the illumination of selective light (AM 1.5 and $\lambda > 525$ nm) at 0.6 V versus RHE. The difference between the activity of pristine BiVO₄ and Au-BiVO₄ shows the total enhancement. The activity at above 525 nm is attributed to the plasmonic enhancement effects. (b) Finite-difference time-domain (FDTD) simulation of the electric field distribution at the interface of a single spherical Au NP and BiVO₄.

photocurrents between Au-BiVO₄ and pristine BiVO₄ under solar illumination depicts the overall enhancement. To further analyze the plasmonic effects, we used a 525 nm long-pass filter attached to the solar simulator. The photocurrent observed in this case is derived from the plasmon-enhanced light absorption, PRET and the hot-electron injection because pristine BiVO₄ has no activity above 525 nm. Since the LSPRs are sensitive to the shape and size of Au NPs, it is possible to extend the absorption to the entire visible range by the incorporation of different types of NPs such as Au nanorods [40].

To further understand the PEC enhancements in the Au-BiVO₄ electrodes, we studied the plasmon-enhanced electromagnetic field using the FDTD method. The electromagnetic response of the hybrid electrodes, as shown in

figure 4(b), is dominated by local 'hot spots'. The main intense local fields in one Au NP can be seen in the figure, which shows the electric field distribution of the hot spot regions. In this local hot spot region, the electric field intensity at the BiVO₄ surface is ∼5 times higher than that of the incident electric field intensity. This indicates that the photon absorption rate (and hence $e^- - h^+$ pair generation rate) is much higher than for pristine BiVO₄. The penetration length of field enhancement into the BiVO₄ is ∼30 nm. Thus, a higher carrier generation resulting from hot-electron injection, PRET, and electromagnetic field enhancement is observed in the Au-BiVO₄ photoanode. Further, the nanoporous architecture aids in the efficient utilization of $e^- - h^+$ pairs. The $e^- - h^+$ pairs are readily separated under the influence of the surface potential and their travel distance to the BiVO₄ surface is shortened. Last but not least, the co-catalyst effect of Au for water oxidation should also be considered [45]. However, with the dominant plasmonic enhancement component for the incident light above 525 nm (figure 4(a)), the co-catalyst component has a relatively lower contribution than the plasmonic effects. Thus, a combination of higher e^--h^+ pair generation and efficient charge separation leads the PEC performance to be far superior to previously reported systems with a similar configuration [35, 36, 38].

Figure 5 depicts a pictorial model of the plasmonic enhancement mechanism. When the photoanode absorbs light with energies above the band gap of BiVO₄, the photoelectrons generate and move to the CB of BiVO₄. Simultaneously, Au NPs absorb the incident irradiation, generate hot electrons, and strengthen the electromagnetic field at the metal-semiconductor interfaces. These hot electrons are injected over the Schottky barrier into the CB of BiVO₄ [46], and eventually move on to the cathode where they interact with protons to form hydrogen [32, 47]. Being a metal, Au consists of free electrons with a lack of holes. With the continuous plasmonic hot-electron injection, excited Au NPs undergo redox reactions evolving hydrogen and oxygen from water. At the bottom of the CB, additional vacancies are formed by the plasmon-induced electromagnetic field. These vacancies facilitate the generation of photoelectrons by direct excitation. This electromagnetic field is not uniform on the plasmonic metal surface, so the formation of electron-hole pairs should be larger in the region of semiconductors closest to the Au NPs. The surface potential promotes the separation of $e^- - h^+$ pairs and shortens their distance to travel to the surface of BiVO₄.

In order to confirm that the photocurrent generated is exclusively for water splitting rather than any other undesired side reactions, both hydrogen and oxygen evolution tests of the assembled PEC cell were performed (figure 6). The ratio of evolution rates of H₂ and O₂ is close to the stoichiometric value of 2.0, with rates of 68.72 ± 0.05 μmol h⁻¹ cm⁻² for H₂ and 35.15 ± 0.05 μmol h⁻¹ cm⁻² for O₂. Assuming a 100% Faradaic efficiency, the evolution rates of H₂ and O₂ should be 72.38 μmol · h⁻¹ · cm⁻² and 36.19 μmol h⁻¹ cm⁻², respectively, for Au-BiVO₄ (12 h) at an average photocurrent of 3.88 mA cm⁻². Similarly, the theoretical (and actual) amount of pristine BiVO₄ gas evolution is 12.94 μmol h⁻¹
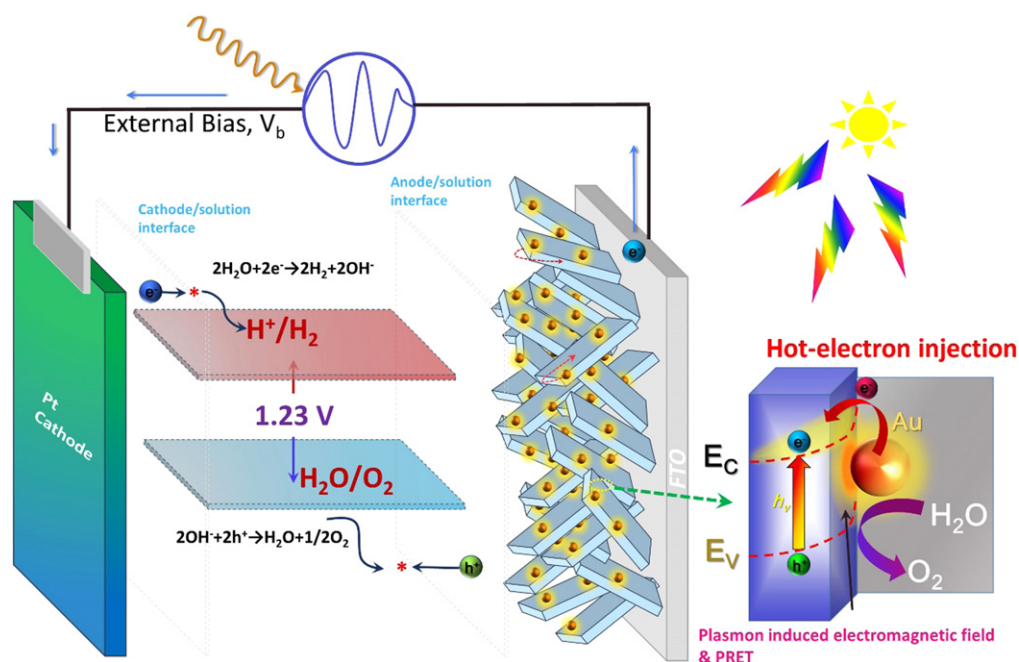
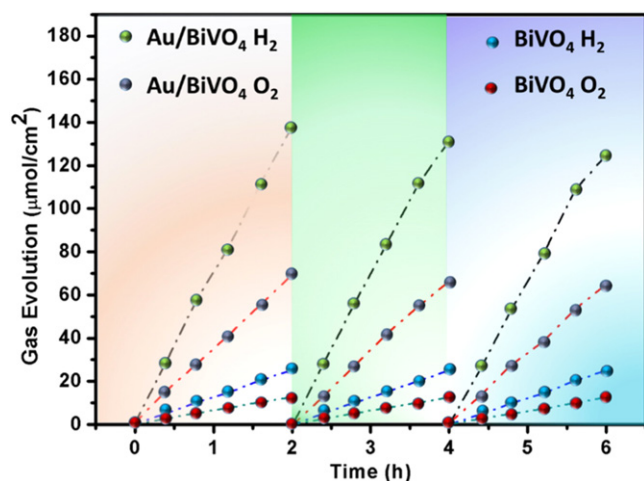**Figure 5.** Schematic illustration of plasmonic effects in the Au-BiVO$_4$ photoanodes for solar water splitting.

Figure 6. Time courses of H$_2$ and O$_2$ evolution for Au-BiVO$_4$ (12 h) and BiVO$_4$ photoelectrodes under an AM 1.5G solar simulator in a 0.2 M Na$_2$SO$_4$ aqueous solution at an applied bias of 1.0 V versus RHE.

Conclusions

We have developed nanoporous Au-BiVO$_4$ photoanodes with a high surface area, short carrier-diffusion length, and plasmonic enhancements for efficient PEC water splitting applications. We have analyzed the different plasmonic effects of Au NPs in the photoanodes. Through the mechanistic study, we have established that the plasmon-induced hot-electron injection, PRET and plasmon-enhanced electromagnetic field are major influences on the plasmonic effects. Moreover, other factors like the catalytic effect of Au also contribute to the PEC performance. We have found that there is an optimal deposition time of Au NPs on the BiVO$_4$, which will balance the plasmonic enhancements and blocking effect of the Au NPs. The Au-BiVO$_4$ photoanodes exhibit five times higher AM 1.5G photocurrents than pristine BiVO$_4$ with over 95% total Faradaic efficiency. It is worth noting that the commendable performance was achieved without the incorporation of any oxygen evolution catalyst or any other metal doping. Our nanoporous Au-BiVO$_4$ electrodes with their efficient PEC performance and long-term stability will pave the way towards industrial applications for solar water oxidation via the efficient utilization of the solar spectrum.

cm^{-2} (12.76 μmol h^{-1} cm^{-2}) for H$_2$ and 6.471 μmol h^{-1} cm^{-2} (6.285 μmol h^{-1} cm^{-2}) for O$_2$. Consequently the Faradaic efficiencies for both gases are higher than 95%, indicating that the observed photocurrent can be fully attributed to water splitting. The enhancements can arise from both the plasmonic effects and the catalytic effect of Au. Notably, the photocurrents possess a minimal decay of less than 5% in the long-term test (see figure S7), implying the high stability of the as-prepared photoanodes. The decay at the higher photocurrent is due to O$_2$ bubble trapping within the nanostructure of BiVO$_4$.

Experimental section

Fabrication of BiVO$_4$ electrodes

All the reagents were of analytical grade and used without further purification, and deionized water was used in all experiments. Nanoporous BiVO$_4$ films were synthesized on a FTO glass substrate with nanostructured BiOI films as templates using an electrodeposition method reported previously

[8]. Briefly, 50 ml 0.8 M $Bi(NO_3)_3$ and 8 M KI (pH = 1.7) were added to 20 ml of 0.23 M p-benzoquinone absolute ethanol solution. Pt wire and saturated Ag/AgCl were used as the counter electrode and reference electrode in all the electrochemical experiments. The cathodic deposition was carried out potentiostatically at −0.14 V for 3 min. The resulting BiOI precursor films were further pipetted with 150 μl of 0.2 M $VO(acac)_2$ in dimethyl sulfoxide (DMSO) and annealed at 450 °C for 2 h. Afterwards, the films were washed by soaking them in 1 M NaOH solution for 30 min. Finally, the resulting nanoporous $BiVO_4$ electrodes were rinsed with deionized water and dried at room temperature.

Decoration of BiVO4 electrodes with Au NPs

The colloidal Au NPs were prepared in a mixed solution of 25 ml of sodium citrate (1%) and 250 ml of Au metal salt ($HAuCl_4$, 0.4 mM) solution. The solution was heated up to 90 °C for 15 min and then cooled down. The as-prepared $BiVO_4$ substrates were immersed in the solution for variable durations. Following this, the sample was thoroughly washed by deionized water, and dried at room temperature. Finally, the samples were annealed in an ambient environment at 350 °C for 1 h to generate Au NPs on the surface of the nanoporous $BiVO_4$.

Characterization

The structures and compositions of the samples were characterized with a SEM (FEI Quanta 650) integrated with an EDS detector and XRD (Rikagu MiniFlex 600). Total transmittance and diffuse reflectance spectra were measured with a Cary 500 UV-vis-NIR spectrophotometer attached to a Labsphere DRA-CA-5500 integrating sphere.

PEC measurements and analyses

PEC measurements were conducted in a three-neck glass electrode cell with the sample being measured as the working electrode. The illumination source was a 150 W Xe arc lamp (Newport, 6255) directed at the quartz PEC cell (100 mW cm^{-2}). All the electrochemical measurements were performed on a CHI 660E electrochemical workstation at room temperature. The gas evolution was conducted at the same conditions with a bias of +1.0 V versus RHE.

The IPCE was calculated according to the following equation:

$$\mathrm{IPCE}(\lambda) = \frac{1240J(\lambda)}{\lambda \times P(\lambda)} \times 100\% \qquad (1)$$

where λ is the wavelength (nm), $J(\lambda)$ is the photocurrent density (mA cm^2), and P(λ) is the incident power density of the monochromated light (mW cm^2). The solar energy-conversion efficiency, (η), was calculated from the experimental J–V curves by assuming 100% Faradaic efficiency according to the following equation:

$$\eta(\lambda) = \frac{|J| \times (1.229 - V_{\mathrm{bias}})}{P_{\mathrm{in}}} \times 100\% \qquad (2)$$

where J is the photocurrent density (mA cm^2), P_{in} is the incident illumination power density (AM 1.5G, 100 mW cm^{-2}) and V_{bias} is the applied bias versus RHE (V).

Numerical simulations

The numerical simulations were performed with Lumerical, a commercial FDTD Maxwell equation solver. Based on experimental measurements, a spherical Au NP (diameter = 30 nm) was attached onto the surface of a $BiVO_4$ nanoplate of 70 × 100 × 100 nm. Linearly polarized light is illuminated normally onto the substrate, with the polarization normal to the interface between the Au NP and the $BiVO_4$. The reflectance light and electromagnetic field were collected with a 2D frequency-domain power detector and an electric field detector at the top, respectively, at a wavelength of 543 nm.

Acknowledgments

References

[1] Osterloh F E 2013 Chem. Soc. Rev. 42 2294
[2] Noh S Y, Sun K, Choi C, Niu M, Yang M, Xu K, Jin S and Wang D 2013 Nano Energy 2 351
[3] Fujishima A and Honda K 1972 Nature 238 37
[4] Shen S, Jiang J, Guo P, Kronawitter C X, Mao S S and Guo L 2012 Nano Energy 1 732
[5] Liu J, Liang C, Xu G, Tian Z, Shao G and Zhang L 2013 Nano Energy 2 328
[6] Yang X, Wolcott A, Wang G, Sobo A, Fitzmorris R C, Qian F, Zhang J Z and Li Y 2009 Nano Lett. 9 2331
[7] Cheng C, Zhang H, Ren W, Dong W and Sun Y 2013 Nano Energy 2 779
[8] Kim T W and Choi K-S 2014 Science 343 990
[9] Walsh A, Yan Y, Huda M N, Al-Jassim M M and Wei S-H 2009 Chem. Mater. 21 547
[10] Park Y, McDonald K J and Choi K-S 2013 Chem. Soc. Rev. 42 2321
[11] Zhong D K, Choi S and Gamelin D R 2011 J. Am. Chem. Soc. 133 18370
[12] Abdi F F, Firet N and van de Krol R 2013 Chem. Catal. Chem. 5 490
[13] Seabold J A, Zhu K and Neale N R 2014 Phys. Chem. Chem. Phys. 16 1121
[14] Karuturi S K, Cheng C, Liu L, Su L T, Fan H J and Tok A I Y 2012 Nano Energy 1 322

[15] Shi X J, Choi Y, Zhang K, Kwon J, Kim D Y, Lee J K, Oh S H, Kim J K and Park J H 2014 *Nat. Commun.* **5** 4775

[16] Pihosh Y *et al* 2015 *Sci. Rep.* **5** 11141

[17] Gan J, Lu X, Rajeeva B B, Menz R, Tong Y and Zheng Y 2015 *Chem. Electro. Chem.* **2** 1385

[18] Mubeen S, Lee J, Singh N, Krämer S, Stucky G D and Moskovits M 2013 *Nat. Nanotechnol.* **8** 247

[19] Gao C, Hu Y, Wang M, Chi M and Yin Y 2014 *J. Am. Chem. Soc.* **136** 7474

[20] Brolo A G 2012 *Nat. Photonics* **6** 709

[21] Zheng Y B, Jensen L, Yan W, Walker T R, Juluri B K, Jensen L and Huang T J 2009 *J. Phys. Chem.* C **113** 7019

[22] Kumar R, Zhou H and Cronin S B 2007 *Appl. Phys. Lett.* **91** 223105

[23] Zheng Y B, Payton J L, Song T-B, Pathem B K, Zhao Y, Ma H, Yang Y, Jensen L, Jen A K-Y and Weiss P S 2012 *Nano Lett.* **12** 5362

[24] Oulton R F, Sorger V J, Zentgraf T, Ma R-M, Gladden C, Dai L, Bartal G and Zhang X 2009 *Nature* **461** 629

[25] Hu M, Chen J, Li Z-Y, Au L, Hartland G V, Li X, Marquez M and Xia Y 2006 *Chem. Soc. Rev.* **35** 1084

[26] Gao C, Lu Z, Liu Y, Zhang Q, Chi M, Cheng Q and Yin Y 2012 *Angew. Chem. Int. Ed.* **51** 5629

[27] Boltasseva A and Atwater H A 2011 *Science* **331** 290

[28] Hou W and Cronin S B 2013 *Adv. Funct. Mater.* **23** 1612

[29] Warren S C and Thimsen E 2012 *Energ. Environ. Sci.* **5** 5133

[30] Chen H M, Chen C K, Liu R-S, Zhang L, Zhang J and Wilkinson D P 2012 *Chem. Soc. Rev.* **41** 5654

[31] Gao H, Liu C, Jeong H E and Yang P 2011 *ACS Nano* **6** 234

[32] Tian Y and Tatsuma T 2005 *J. Am. Chem. Soc.* **127** 7632

[33] Schaadt D, Feng B and Yu E 2005 *Appl. Phys. Lett.* **86** 063106

[34] Liu Z, Hou W, Pavaskar P, Aykol M and Cronin S B 2011 *Nano Lett.* **11** 1111

[35] Xie S, Li M, Wei W, Zhai T, Fang P, Qiu R, Lu X and Tong Y 2014 *Nano Energy* **10** 313

[36] Chen H M, Chen C K, Chen C-J, Cheng L-C, Wu P C, Cheng B H, Ho Y Z, Tseng M L, Hsu Y-Y and Chan T-S 2012 *ACS Nano* **6** 7362

[37] Thimsen E, Le Formal F, Grätzel M and Warren S C 2010 *Nano Lett.* **11** 35

[38] Zhang L, Lin C Y, Valev V K, Reisner E, Steiner U and Baumberg J J 2014 *Small* **10** 3970

[39] Cao S-W, Yin Z, Barber J, Boey F Y, Loo S C J and Xue C 2011 *ACS Appl. Mater. Inter.* **4** 418

[40] Pu Y-C, Wang G, Chang K-D, Ling Y, Lin Y-K, Fitzmorris B C, Liu C-M, Lu X, Tong Y and Zhang J Z 2013 *Nano Lett.* **13** 3817

[41] Chae S Y, Jung H, Jeon H S, Min B K, Hwang Y J and Joo O-S 2014 *J. Mater. Chem.* A **2** 11408

[42] Zhao J, Pinchuk A O, McMahon J M, Li S, Ausman L K, Atkinson A L and Schatz G C 2008 *Acc. Chem. Res.* **41** 1710

[43] Kelly K L, Coronado E, Zhao L L and Schatz G C 2003 *J. Phys. Chem.* B **107** 668

[44] Burda C, Chen X, Narayanan R and El-Sayed M A 2005 *Chem. Rev.* **105** 1025

[45] Primo A, Marino T, Corma A, Molinari R and Garcia H 2012 *J. Am. Chem. Soc.* **134** 1892

[46] Cooper J K, Gul S, Toma F M, Chen L, Glans P A, Guo J H, Ager J W, Yano J and Sharp I D 2014 *Chem. Mater.* **26** 5365

[47] Lee J, Mubeen S, Ji X L, Stucky G D and Moskovits M 2012 *Nano Lett.* **12** 5014